Sensors & Actuators: B. Chemical 380 (2023) 133346

Contents lists available at ScienceDirect

Sensors and Actuators: B. Chemical

journal homepage: www.elsevier.com/locate/snb

Ti@MoS_2 incorporated Polypropylene/Nylon fabric-based porous, breathable triboelectric nanogenerator as respiration sensor and ammonia gas sensor applications

Sushmitha Veeralingam, Sushmee Badhulika *

Department of Electrical Engineering, Indian Institute of Technology Hyderabad, Hyderabad 502285, India

ARTICLE INFO

Keywords:
MoS_2
Triboelectric nanogenerator
Ammonia gas sensor
Respiration sensor
Energy harvester

ABSTRACT

High output and non-interrupted power supply from fabric-based nanogenerators still remain a major challenge in developing self-powered wearable electronic applications. Addressing this, we demonstrate a low-cost, lead-free triboelectric nanogenerator based on hydrothermally grown Titanium (Ti) functionalized Molybdenum Disulfide (MoS_2) interspersed polypropylene (PP) cloth and sandwiched with Nylon cloth for a highly sensitive respiration sensor and self-powered ammonia gas sensor. The nanogenerator with the device configuration Cu/Ti@MoS_2/PP: Nylon /Ag is attached to a respiratory mask, and the open-circuit voltage (V_{oc}) and short-circuit current density (J_{SC}) during respiration cycles were obtained as 29.3 V and 42.7 μA/cm^2 respectively. A significant difference in the breath pattern of human respiration cycles. Further, a fully self-powered ammonia gas sensor was demonstrated by integrating the triboelectric nanogenerator with Ti@MoS_2/PP ammonia sensor. The self-powered Ti- MoS_2 on PP cloth-based gas sensor driven by TENG displays an excellent response with a wide dynamic sensing range of ammonia gas from 200 ppb to 2600 ppb at room temperature, with a high sensitivity, selectivity and a rapid response time. This study explores the bifunctional nature of Ti@MoS_2 nanoparticles as a respiratory mask and a self-powered ammonia gas sensor fabricated with excellent potential for self-powered health diagnostic applications.

1. Introduction

Demand in the power supply due to advancement in portable electronics devices gives rise to energy harvesting from the non-renewable source of energy to avoid carbon emission from fossil energy [1]. Piezoelectric nanogenerator can generate energy from human motion like walking, running, eye blinking, chewing, snoring etc., and can charge a battery to drive the low power LED, pH sensor [2], photodetector [3], and wearable electronic devices. Low power supply generation of piezoelectric nanogenerator restricts its use in high-power wearable electronics devices. In this regard, the triboelectric nanogenerator is being widely used due to its very high output power, simple production, and high conversion efficiency, which is sufficient to power small electronic devices, high power LED.

Generally, every material exhibits triboelectric properties including metals, polymers, silk, wood, plastic etc, wherein, the classification is done based on the affinity of the material towards electrons [4]. Recently, Seol et al. explored the triboelectric charging behaviors of various 2D nanomaterials and their higher tendency to gain electrons. Thus, 2D nanomaterials like graphene [5], MXene [6], black phosphorous [7], h-BN [8], layered MOFs can be located near the negative side of the triboelectric series. Although, many ultrathin 2D nanomaterials have been prepared and studied, the output performances were limited. Hence, it is necessary to improve the electrical output performance of the 2D-TENGs by i) Surface modification of triboelectric layers, and ii) development of novel nanostructures for enhancing the charge density.

In addition, TENGs could be effectively utilized to harvest biomechanical energy [9] and convert mechanical stimuli to electrical signals [10] for self-powering various devices like gas sensors [11] pressure sensors [13], and tactile sensors [14] without the necessity of additional power supplies. However, most gas sensors are integrated with the TENGs as one device [15], which sometimes results in the generation of noise signals and leads to generation of unreliable data. TENG can be effectively used as a self-powering unit for gas sensors wherein the response from the gas sensor can be precisely measured independently.

In this regard, here we fabricate the flexible triboelectric

* Corresponding author.
E-mail address: sbadh@iith.ac.in (S. Badhulika).

https://doi.org/10.1016/j.snb.2023.133346
Received 20 December 2022; Accepted 10 January 2023
Available online 11 January 2023

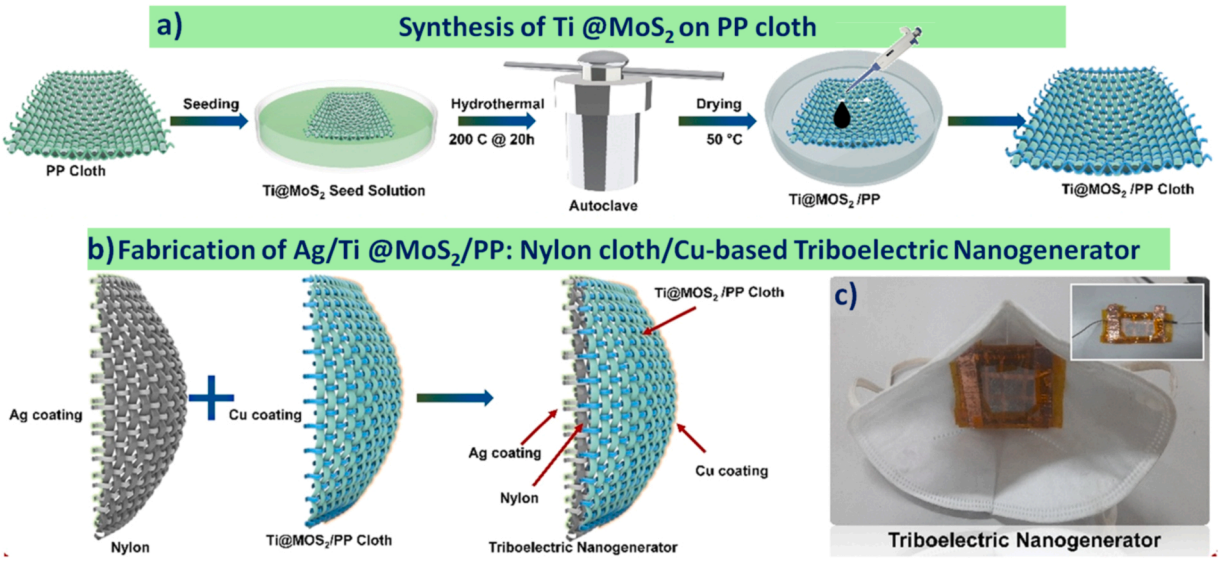

Fig. 1. **(a)** Synthesis of Ti@MoS_2 on PP Cloth **(b)** Steps for the fabrication of Ag/Ti@MoS_2:PP/Nylon/Cu Triboelectric Nanogenerator **(c)** Real-time representation of triboelectric mask nanogenerator.

nanogenerator using PP and Nylon cloth for energy harvesting applications. This nanogenerator is fixed inside the N95 mask and used for powering the gas sensor. The Ti functionalized MoS_2 was grown on the PP cloth which acts as one of the triboelectric layers of the nanogenerator. The Ti@MoS_2@PP: Nylon based triboelectric nanogenerator delivers high open circuit voltage and current density of 10 V and 15 μA/cm^2 during breathing cycles. The fabricated nanogenerator was used to power an ammonia gas sensor fabricated using Ti@MoS_2 grown over PP cloth.

2. Experimental section

2.1. Materials

Silver (Ag; 99.999 %), Copper (Cu; 99.999 %), Polytetrafluoroethylene (PTFE), Nylon fabric, Titanium dioxide, sodium molybdate and thiourea were procured from Sigma Aldrich. PP cloth was taken from garment shop with a GSM of 25.

2.2. Synthesis of Ti -MoS_2 and Ti@MoS_2/PP cloth

Fig. 1**(a)** shows the schematic of the synthesis of Ti-MoS_2 on PP cloth. Ti – MoS_2 was synthesized using Hydrothermal technique. The seed solution was prepared by adding 1 mM of sodium molybdate, 2 mM of thiourea and 0.338 μM of Titanium dioxide in DI water. Following which, a separate 30 mL Teflon lined reactor consisting of 1 M of Sodium Molybdate, 2 M of thiourea and 3.38 μM of Titanium dioxide in DI water was maintained at 200 °C for 20 h. The reactor was allowed to cool down at room temperature. The obtained Ti- MoS_2 was uniformly dispersed in ethanol and deposited onto the PP cloth and was dried at 50 °C for 2 h.

2.3. Fabrication of Cu and Ag electrodes

Copper (Cu) and Silver (Ag) metal electrode were thermally coated on Ti@MoS_2/PP cloth and nylon cloth respectively, under a high vacuum of 10^{-6} Torr. Cu and Ag powder (99.999 %) were thermally evaporated with a deposition rate of 1 nm/s for 50 s to acquire a uniform thickness of electrodes.

2.4. Fabrication of Ti@MoS_2/PP:Nylon triboelectric nanogenerator

Ti@MoS_2/PP: Nylon-based triboelectric nanogenerator was fabricated using a simple sandwiching of Cu/Ti@MoS_2/PP with Nylon /Ag as shown in Fig. 1**(b)**. The deposited Cu on the Ti@MoS_2: PP film was placed over Ag coated Nylon film and the connection was taken from the Cu and Ag electrodes. The digital image of the triboelectric mask nanogenerator is shown in the Fig. 1**(c).**

3. Results and discussion

3.1. Structural and morphological analysis

3.1.1. Ti functionalized MoS_2

XRD spectroscopy was used to study the crystal structure of Ti@MoS_2 nanoparticles. XRD spectra shows in Fig. S2(a) confirms the trigonal phase of Ti@MoS_2 nanoparticles with lattice parameters a = 0.316, b = 0.316, c = 1.864 nm, α = 90°, β = 90°, γ = 120°. The sharp peaks centered at 14.14, 33.18, 39.62, 44.54, 51.42, 58.34, 65,04, 78.22 corresponds to (002), (100), (103), (006), (105), (110), (008) and (205) respectively which is well indexed with the JCPDS 37-1492 (*P63/mmc*) [8]. The peak position indicates that the Ti atom replaces the position of Mo in the MoS_2 crystal structure without distorting the crystal structure [9]. The trigonal phase crystal structure of Ti@MoS_2 nanoparticles is shown in Fig. S2(b) in which Ti atoms occupies the position of Mo atom in MoS_2 lattice.

The Raman spectroscopy is used to study the functional group present in the Ti functionalized MoS_2 system. Fig. S2(c) shows the Raman spectra with two high intense peaks centered at 380.9 cm^{-1} and 401.1 cm^{-1} which is attributed to the $E^1_{2\,g}$ and $A_{1\,g}$ vibration of MoS_2 respectively. Peak 380.9 cm^{-1} corresponds to the in-plane vibration of Mo-S or Ti-O functional groups. Peak 401.1 cm^{-1} attributes to the out-of-plane vibration of Mo-S or Ti-O functional groups. It is clearly seen that the Ti doping does not affect the band position of $E^1_{2\,g}$ and $A_{1\,g}$ modes due to acoustic modes of vibration nature of Ti. This resonance mismatched between the atoms due to electron-pulling effect give rise to distortion in the peak intensities as observed in case of $E^1_{2\,g}$ mode, as minority of negative charged electrons were available for the Raman scattering [10].

The surface morphology and topography of Ti functionalized MoS_2 nanoparticles was also analyzed using FE-SEM. Fig. S2(d) shows the nano-flower type morphology is distributed throughout the surface. To know the minute details of Ti functionalized MoS_2 nanoparticles the magnified image was also shown in Fig. S2(e). Ti functionalized MoS_2 nanoparticles has the average diameter of (240 + 20) nm and these

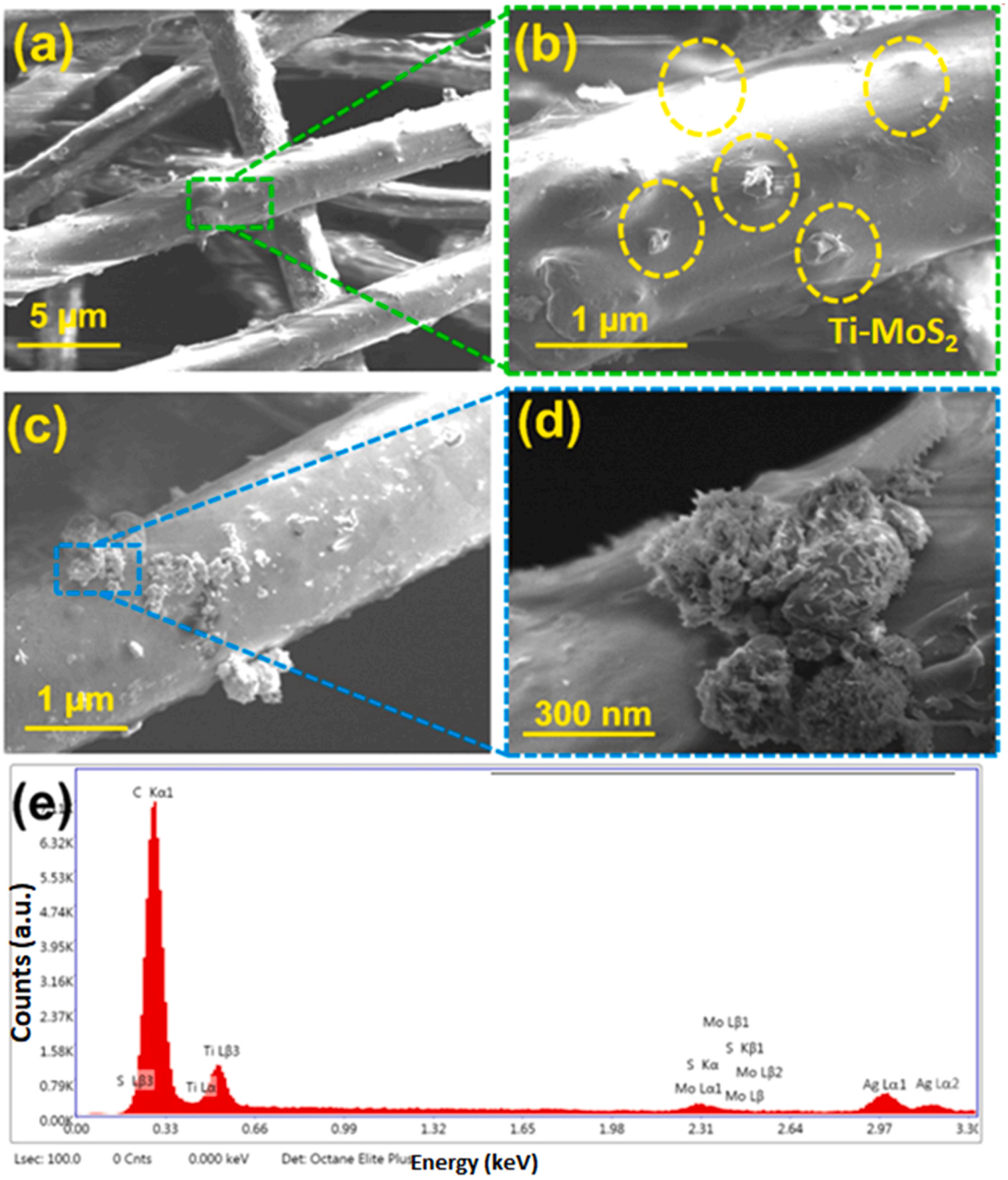

Fig. 2. **a)** Low magnification image of Ti@MoS_2 coated PP cloth. **(b)** and **(c)** High magnification image of Ti@MoS_2 coated PP cloth. **(d)** High-resolution images of Ti@MoS_2 coated over a PP cloth. **(e)** EDS of as synthesized Ti@MoS_2 coated PP cloth.

nanoflower consist of the agglomerated nano-flakes particles with the average thickness (30 + 20) nm. The nano-flower also contains the vertically aligned hexagonal shaped nanorods was observed, which is due to the presence of Ti doping in the MoS_2 crystal structure. The c-axis grow hexagonal atomic orientation nanorods has average length of (560 + 60) nm and diameter of (65 + 10) nm. High surface area of Ti functionalized MoS_2 nano-flakes will be good for gas sensor and triboelectric applications due to increased interacting sites.

3.1.2. *Ti@MoS_2 interspersed PP cloth*

The microstructural analysis of synthesized triboelectric material was also observed using FE-SEM. Fig. 2**(a)** shows the low magnification image of Ti@MoS_2 coated PP cloth. It is evident that the Ti@MoS_2 nanoflowers were coated over the PP cloth. High magnification image of PP microfibers was also recorded as shown in Fig. 2**(b)**. Fig. 2**(c)** shows that the Ti@MoS_2 nanoparticles are firmly deposited over the PP microfiber. At high temperature (> 50 °C) the surface of PP become rough which helps in the better interface bonding of Ti@MoS_2 nanoparticles. Fig. 2**(d)** shows the high-resolution images of Ti@MoS_2 coated over a PP microfiber where it is clearly seen that the Ti functionalized MoS_2 nanoparticles consist of nanoflakes and nanorods structures were interspersed onto the PP microfibers. Energy Dispersive X-Ray Spectroscopy was also performed to study the elemental analysis of as synthesized Ti@MoS_2 coated PP cloth. It is confirmed from the Fig. 2**(e)** that there is a presence of C, F, Ti, Mo, Ag and S elements in the system.

Silver (Ag) and Copper (Cu) has been used as a conductive electrode

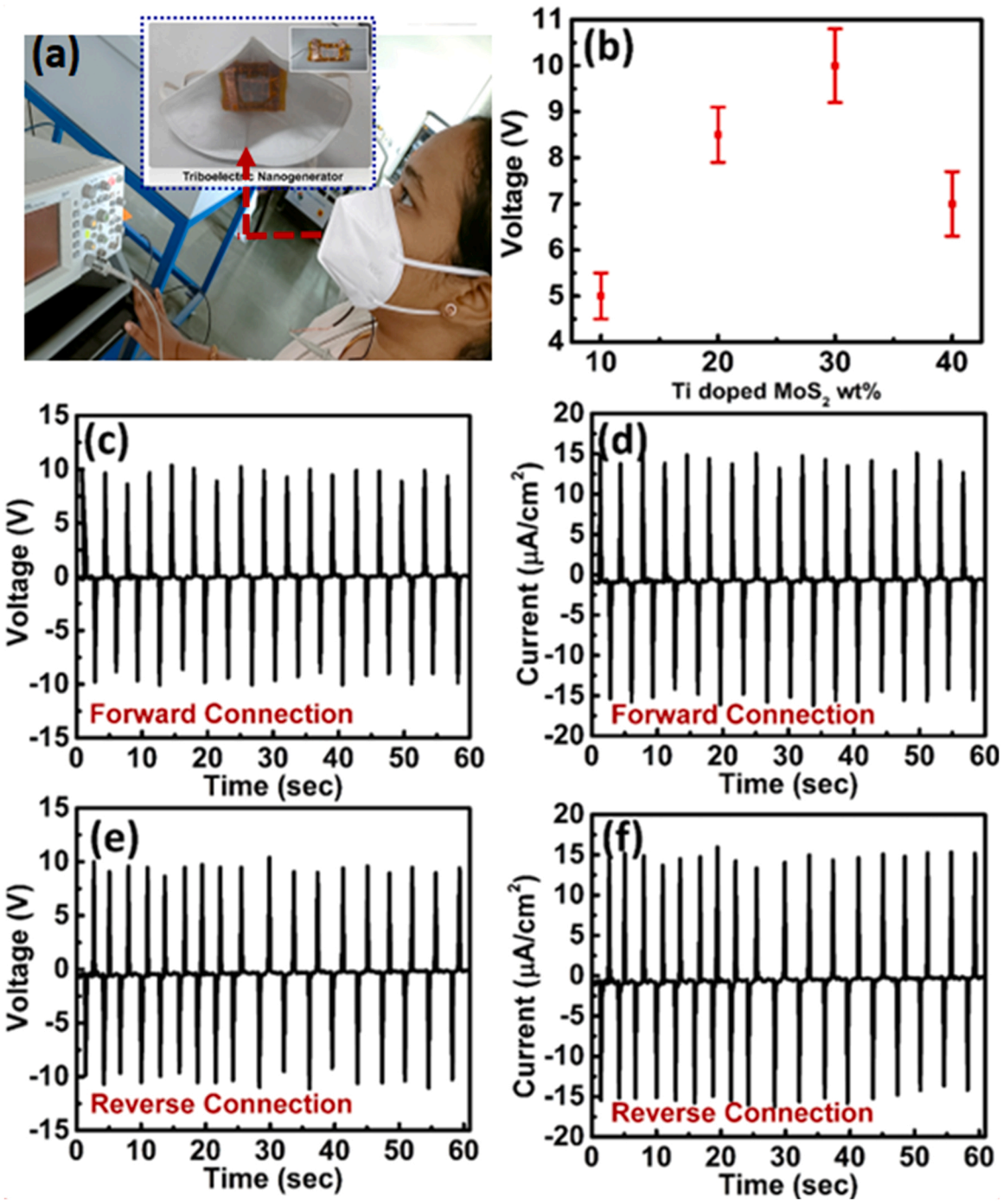

Fig. 3. **(a)** Fabric based flexible nanogenerator with optimized device configuration Ag/(Ti@MoS_2:PP)/Nylon/Cu and inset shows the pictorial representation of nanogenerator attached to the mask. **(b)** Open circuit voltage for different wt% of Ti-MoS_2. Forward connection **(c)** open circuit voltage and **(d)** current density of Ti@MoS_2:PP/Nylon based triboelectric nanogenerator. Reverse connection **(e)** open circuit voltage and **(f)** current density of triboelectric nanogenerator driven by human breath.

of PP: Nylon based flexible triboelectric nanogenerator with high sheet resistance of 11 Ω/sq and 8 Ω/sq respectively. Fig. 3**(a)** shows the fabric based flexible nanogenerator with device configuration Ag/(Ti@MoS_2:PP)/Nylon/Cu and the pictorial representation of nanogenerator attached to the mask is shown in the inset of Fig. 3**(a)**. The triboelectric nanogenerator was fabricated at different wt% concentration (10 wt%, 20 wt%, 30 wt% and 40 wt%) of Ti@MoS_2 over the PP cloth and output performance were recorded. The triboelectric nanogenerator was attached with the mask and the output performance was recorded during normal respiration rate.

3.2. Output performance of Ti@MoS_2/PP/Nylon based triboelectric nanogenerator

The output performance of the Ti@MoS_2:PP/Nylon based triboelectric nanogenerator for 4 devices is shown in Fig. 3**(b)**. Open circuit voltages of 5 V, 8.5 V, 10 V and 7 V were observed at different concentration of 10 wt%, 20 wt%, 30 wt% and 40 wt% respectively. Rise in the open circuit voltage of nanogenerator was observed to increase upto 30 wt% due to the high dielectric constant of Ti@MoS_2:PP [11]. This effect assists in separation of charge carriers and thus increase in the

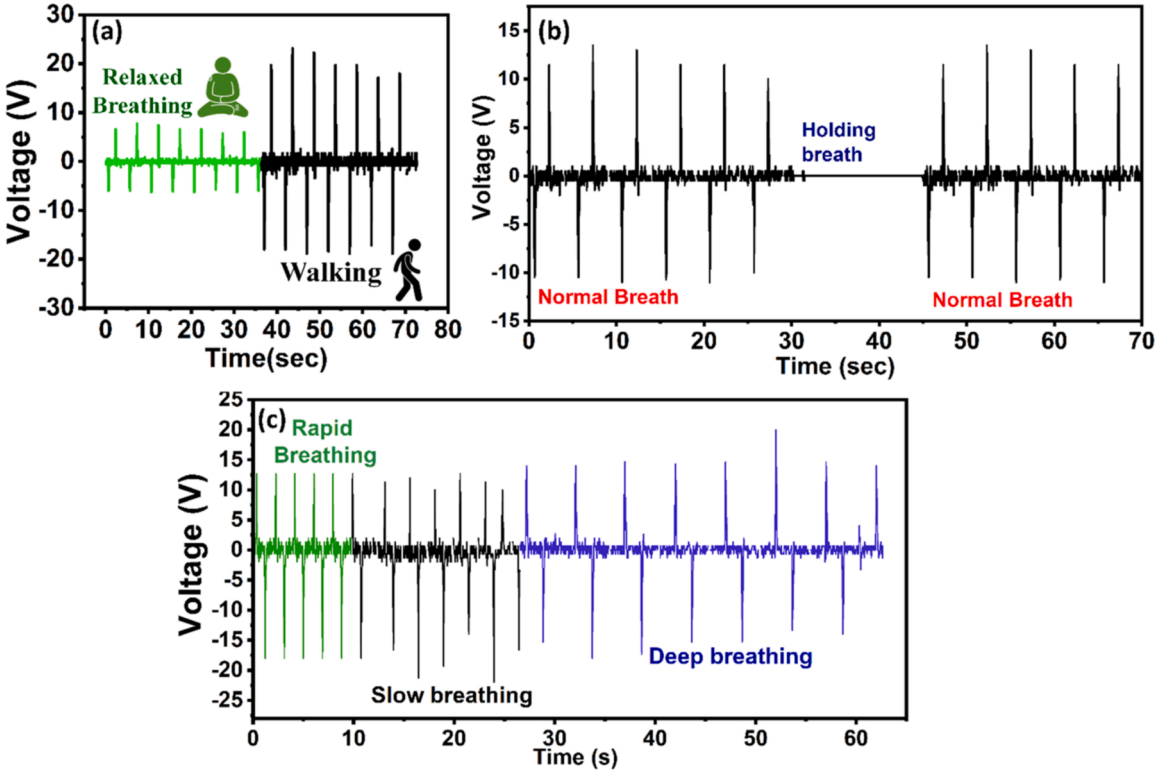

Fig. 4. Realtime breathing application of the Ti@MoS_2: PP/Nylon fabric during a) relaxed breathing and walking b) normal breathing and holding cycle c) Rapid, slow and deep breathing cycles.

Table 1
Comparison of output performance of fabricated Ti@MoS_2/PP: Nylon based nanogenerator with recent reported fabric based triboelectric nanogenerators.

Sr. no.	Materials used	Application	Output performance		Refs.
			Voltage (Open-Circuit) (V)	Current/ Current Density (Short-Circuit)	
1.	CNTs@SF core-sheath fiber fabric	Smart clothing	17	7 μA	[5]
2.	Silicone rubber tube/ stainless steel yarn	Energy textiles	24	1.5 μA	[6]
3.	PTFE/PBT/ Cu/satin weaved fibers	Human motion monitoring	28	0.4 μA	[7]
4.	PVDF nanofibers stitched on nylon fabric	smart glove and joint pads	2	0. 2 μA	[12]
5.	PTFE plain-knitted fabric	Human biomechanical movements	23.50	1.05 μA	[13]
6.	PI-Cu-PET yarn	chest strap for motion monitoring	5	1.6 μA/cm^2	[14]
7.	**Ti@MoS_2/Cu**	**Respiration**	**29.3**	**42.7 μA/ cm^2**	**This work**

CNT – Carbon Nanotube, Ag – Silver, Ti – Titanium, PVA – Polyvinyl alcohol, PET – Polyethylene terephthalate.

output voltage. The output performance decreases with further increase in the concentration beyond 30 wt% concentration which is due to the increase in the conductivity of Ti@MoS_2 on PP cloth and dielectric breakdown effect. 30 wt% concentration of Ti@MoS_2 on PP cloth was therefore considered as optimal wt%.

The output performance of optimized triboelectric mask nanogenerator was recorded for a 27-year-old healthy human subject for 1 min. The open circuit voltage and current graph displayed 17 successive positive and negative peaks. These peaks have been interpreted as the breath rate per minute (BPM) of the healthy subject. The open circuit voltage and current density of 10 V and 15 μA/cm^2 was obtained and the data is shown in Fig. 3**(c)** and **(d)** respectively. The polarity test was also performed by interchanging the connection of electrodes and the same value of open circuit voltage and current density was recorded as shown in Fig. 3**(e)** and **(f)** respectively. Polarity test confirms that the capacitive/charge storage nature of Ti@MoS_2/PP and Nylon cloth is accountable for such high performance.

Further, various configurations were tested to enhance the open circuit voltage of nanogenerator. Multiple similar nanogenerators were cascaded in series connection and in parallel connection to enhance the open circuit voltage and current of nanogenerator as shown in SI Fig. S4**.** The detailed discussion is briefed in the Supplementary information.

The real time applicability of the Ti@MoS_2: PP/Nylon fabric was investigated by subjecting the nanogenerator to different respiration patterns. Initially, the respiration sensor was fixed to the face mask and the subject was allowed to sit in a relaxed position and breath into the sensor for 30 s. The breath pattern in relaxed state induced a low-peak-to-peak voltage of 5 V. During walking conditions, frequent breathing patterns were observed resulting in a larger peak-to peak voltage of 20 V as shown in Fig. 4 **(a)**. Upon breathing i.e., inhalation and exhalation cycle a peak-to-peak voltage of 14 V was observed. When the breathing was stopped and the respiration sensor is taken far away from the nose, no significant peak was observed as shown in Fig. 4**(b)**. Thus, exhibiting the superior sensitivity of the Ti@MoS_2:PP/Nylon based respiration sensor towards human breath. Human respiration behavior was further analyzed by simulating different breath patterns such as rapid breathing, slow breathing, and deep breathing cycles. Different voltage values were

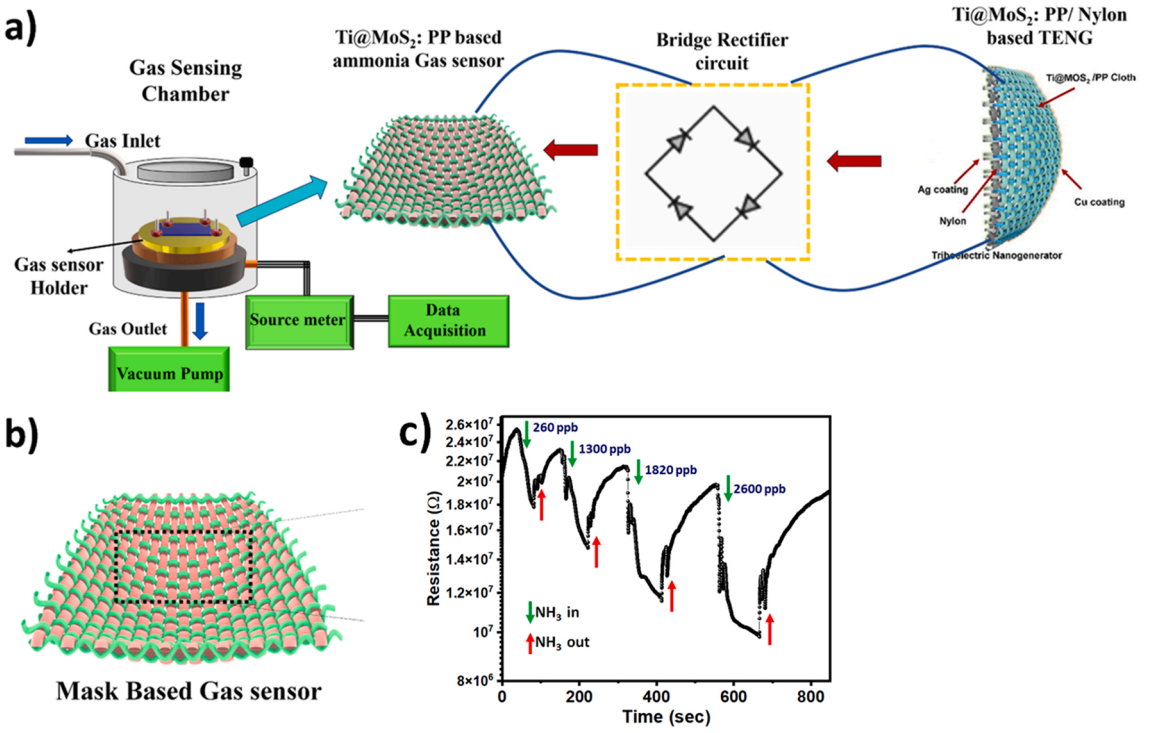

Fig. 5. **(a)** Schematic of the gas sensing chamber and the integrated self-powered ammonia gas sensing setup **b)** Schematic displaying the structure of mask-based gas sensor **c)** The dynamic gas sensing response towards increase in concentrations of ammonia.

recognized for each breath pattern. Rapid breath exhibited a high frequency peak with a lesser peak to peak voltage of 7 V. Slow breath displayed an output peak-to peak voltage of 20 V. During deep breathing cycles an average open circuit voltage of 15 V was observed as shown in Fig. 4**(c)**. Rise in the open circuit voltage of nanogenerator upon breathing can be attributed to the separation of charge carriers. The schematic displaying the working mechanism of Ti@MoS_2:PP/Nylon fabric based triboelectric nanogenerator is shown in Fig. S3**.** The triboelectric nanogenerator works on the vertical contact separation mode. Initially, at steady state condition when no force is applied on the nanogenerator, and the two-triboelectric materials Ti@MoS_2:PP and nylon cloth are apart resulting in zero output. As vertical compression force is applied on the top electrode (Ag coated Ti@MoS_2:PP), the two dielectric films with distinct electron affinity comes in contact with each other [12]. Due to different triboelectric effect and electron affinities of Ti@MoS_2:PP and nylon, the positive charges are generated on Ti@MoS_2:PP side and equal and opposite negative charges are generated on the nylon side of the triboelectric nanogenerator. As external vertical compression force is applied, the two triboelectric material contacts each other, giving rise to potential difference between the top and bottom electrodes [13]. This potential difference drifts the electrons from nylon electrode to Ti@MoS_2:PP electrode resulting in the positive pulse in the output circuit. The electrons get accumulated on the Cu electrode and equal positive charges are generated on the Ag electrode owing to electrostatic induction [14]. Further, when the external pressure is released, the triboelectric surface interaction reduces the electrostatic induction and the accommodated electrons at Ag drift back to the Cu electrode resulting in negative peaks at the output governed by maxwell's displacement current. Sequential to-and-fro motion of triboelectric material owing to contact–separation mode generates the periodic electrostatic potential [15] resulting in the periodic positive and negative peaks of current and voltage across the external circuit.

The comparative analysis of the present work with recently reported fabric based triboelectric nanogenerators is shown in Table 1. In most reports high cost and sophisticated SGA598 Braiding Machine is used to fabricate the triboelectric film of the nanogenerator. In addition, the overall performance of the devices is less. Such low voltages are not sufficient to drive wearable monitoring devices thereby limiting their applications. In contrast, the as-fabricated device in this work delivers a very high open circuit voltage and current density of 29.3 V and 42.7 μA/cm^2 respectively and exhibits high flexibility and biocompatibility.

4. Self-powered gas sensor

The TENG based on Ti-MoS_2:PP/Nylon has potential application value in many fields. In this work, the as- fabricated TENG was used to power an ammonia gas sensor. To study the sensing properties of the self-powered gas sensor, the synthesized Ti-MoS_2:PP gas sensor was integrated with the fabricated Ti-MoS_2:PP/Nylon TENG. The Ti-MoS_2 on PP cloth was connected via a bridge circuitry with the TENG such that the generated AC output from the TENG gets converted to DC power supply. The fabricated gas sensor device was placed in the gas sensing system connected to a four-point probe as shown in Fig. 5**(a)**. The gas-sensing system was stabilized under room temperature and then the gas-sensing experiments were performed by controlling the injection of vapor. The NH_3 vapors were used to perform the gas-sensing; the sensor was placed in a separate chamber such that only the vapors of ammonia were injected via a gas-inlet-tube into the chamber. The schematic of the mask-based gas sensor is shown in the Fig. 5**(b)**. The resistance of the device when exposed to air and the resistance upon exposure to ammonia was measured for different concentrations of ammonia in the range of 260–2600 ppb. The resistance of the gas sensor was found to decrease with increase in the concentration of ammonia as shown in Fig. 5**(c)**. The sensing mechanism of MoS_2-based gas sensors depends on the charge transfer process between target gas molecules and TMDCs materials [16]. The direction of charge transfer depends on oxidizing or reducing nature of target gas analytes. NH_3 is a reducing gas, which tends to donate the lone pair of electrons to the MoS_2. Thus, the resistance of the sensor was found to decrease upon exposure to NH_3. Such charge transfer process has already been verified by theoretical calculation (DFT) [16] and in-situ photoluminescence PL study [17] in

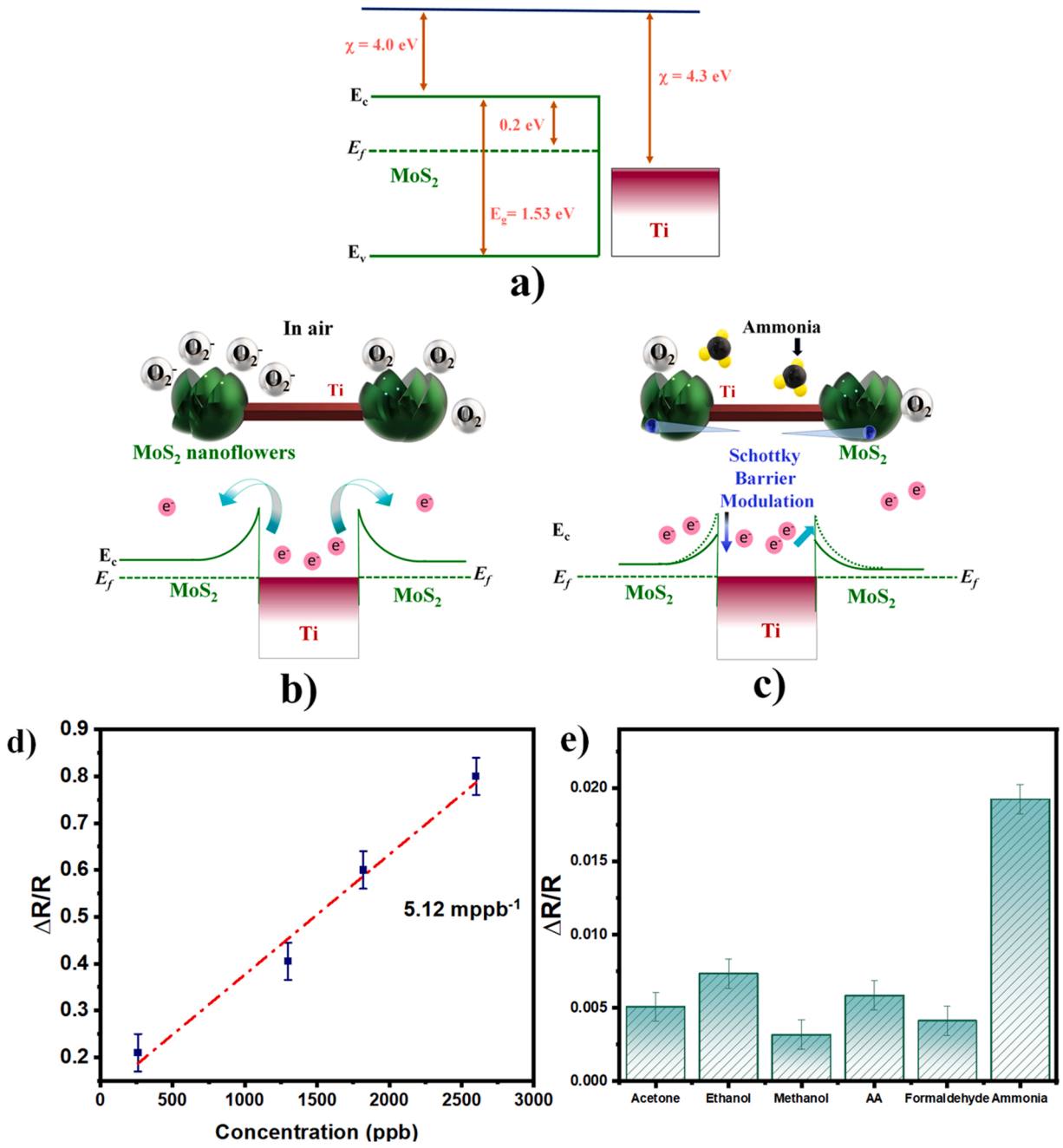

Fig. 6. **(a)** Band diagram of the Ti@MoS_2 structure; Charge transport mechanism and band diagram of the Ti@MoS_2 gas sensor **b)** In air ambient **c)** In Ammonia ambient **d)** Calibration plot of the gas sensor displaying a sensitivity of 0.512 ppb^{-1} **(e)** Selectivity studies towards co-existing species.

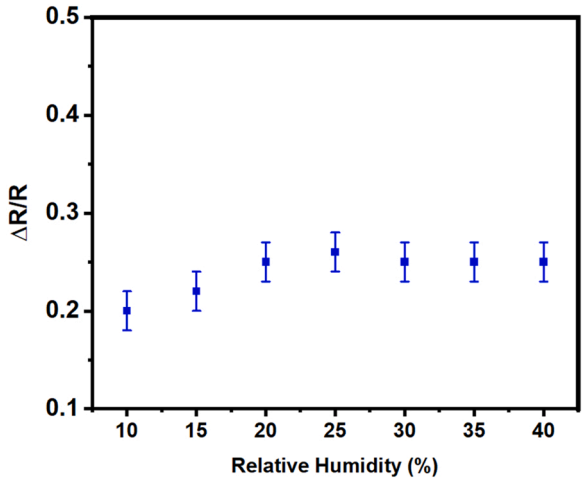

Fig. 7. The change in response of the sensor with respect to relative humidity.

previous reports.

Further, when the surface of Ti-MoS_2 is exposed to ammonia, the NH_3 atoms interacts with the adsorbed oxygen ions and releases the trapped electrons back to the conduction band of Ti@MoS_2 nanoflowers [18]. This leads to an increase in the concentration of electrons in the conduction band of MoS_2. The Ti- functionalization increases the affinity towards NH_3, by acting as an active catalyst by improving the diffusion and transfer of electrons from the adsorbed ammonia to MoS_2.The electrons transfer from Ti to MoS_2, increases the electron density in MoS_2 layer [19]. The band diagram of Ti@MoS_2 is given in the Fig. 6**(a)**. The bandgap of MoS_2 is taken as 1.53 eV, which was calculated using Tauc's plot in our previous work [20]. The electron affinity of MoS_2 and Ti were found to be 4.0 eV and 4.3 eV, respectively [21]. The functionalization of Ti has a significant influence on improving the response and selectivity toward ammonia. The difference in work function between MoS_2 (4.0 eV) and Ti (4.3 eV), results in energy band bending. A depletion region is formed between the metal semiconductor junction, thus inhibiting the charge transfer from the Ti to MoS_2. In air, oxygen molecules get physiosorbed on the surface of MoS_2 to form a schottky barrier as shown in Fig. 6**(b)** and upon injection of NH_3 vapors, the conduction band level of the MoS_2 shifts downward due to the surface charge transfer from NH_3. With the surface charge transfer, the Schottky barrier modulation occurs, which increases the charge transfer from Ti to MoS_2 as depicted in Fig. 6**(c)**. Further, the calibration plot displays a linear response from 260 ppb to 2600 ppb as shown in Fig. 6**(d).** The sensitivity was determined from the slope of the calibration plot as 5.12 % per ppb of NH_3. The limit of detection (LOD) of the NH_3 gas sensor was calculated using;

$$LOD = 3 \times (R_{rms}/\text{slope})$$ [22],

in which R_{rms} is the root-mean-square deviation calculated from the fifth-order polynomial fit of the baseline. LOD of 132 ppb was obtained for the fabricated sensor.

The response of the gas sensor towards interfering gases was also measured to study their cross-response as atmospheric air contains various gases. To evaluate selectivity, the Ti@MoS_2 gas sensor device was subjected to different interfering gases, such as, acetone (800 ppb), ethanol (240 ppb), methanol (400 ppb), acetic acid (48 ppb), and formaldehyde (100 ppb). These interfering gases are commonly found in human exhaled breath with ammonia. The real-time concentrations of each of these gases were obtained from the previous literature [23,24]. The corresponding resistance change of gas sensor when exposed to these different gases is shown in Fig. 6**(e).** Several factors govern the selectivity of a gas sensor such as temperature, gas concentration and unoccupied molecular orbital energy levels [25]. A gas molecule has a unique lowest unoccupied molecular orbital energy. In this case, the electronic energy level of the adsorbed oxygen species on the gas sensor matches with the energy level of NH_3 at room temperature, which enhances the interaction between Ti@MoS_2 and NH_3, thus displaying superior selectivity [25]. The studies displaying the response of the sensor toward the relative humidity have been added to the Fig. 7 below. The gas sensor was placed in the closed chamber, and the relative humidity of the chamber was increased from 10 % to 40 % (with a step of 5 %). Initially, the relative humidity was maintained at 10 % for 5 min, followed by injecting 260 ppb of NH_3 vapors inside the chamber and finally, the corresponding change in resistance was obtained an plotted as shown in figure below. Similarly, the change in resistance was measured for the entire range of humidity values by injecting 260 ppb of NH_3 vapors. All the experiments were carried out at room temperature conditions. The sensor exhibited a minimal change in response when subjected to increased humidity conditions. Thus, clearly indicating the suitability of NH_3 gas sensor at room temperature conditions. The response of the gas sensor was measured for 4 devices, and the estimated error value was found to be less than 1.2 %.

The comparison of the as-fabricated Ti-MoS_2/PP based gas sensor integrated with Ti-MoS_2/PP cloth based nanogenerator is given in comparison Table 2 and detailed explanation is given in Section S7.

5. Conclusion

In summary, a self-powered gas sensor system using Ti@MoS_2 PP/Nylon based TENG was developed, to demonstrate real-time ammonia gas monitoring. A high open circuit voltage and current density of 29.3 V and 42.7 μA/cm^2 respectively were obtained during human respiration cycles. A novel strategy was employed using a bridge rectifier circuit to enable the integration of triboelectric nanogenerator and

Table 2
Comparison of fabricated Ti-MoS_2 based ammonia sensor with recently reported TMDCs based NH_3 sensors.

S. no.	Transition metal dichalcogenide used	Synthesis method	Self-powered	Detection range (ppb)	Response time (s)	Recovery time (s)	Ref.
1	$MoSe_2$	Micromechanical	No	50–500	150	540	[26]
2	Pt-MoS_2	Metal Organic Chemical Vapor Deposition	No	2.5 – 70	300	-	[27]
3	Au-MoS_2	Hydrothermal	No	25–1000	-	-	[28]
4	n-MoS_2/p-CuO	DC magnetron sputtering	No	0–500	17	26	[29]
5	**Ti-MoS_2**	**Hydrothermal**	**YES**	**260–2600**	**51**	**67**	**This work**

gas sensor. The gas sensor enabled the detection of ammonia gas using the Ti@MoS_2 with a response time of 51 s. The gas sensor displayed excellent response towards wide dynamic range of ammonia concentration from 260 ppb to 2600 ppb, with a superior selectivity and sensitivity. The sensing mechanism of ammonia gas upon interaction with Ti@MoS_2 has also been studied extensively. This Ti@MoS_2 based self-powered gas sensor with low cost and high-performance capabilities proves its candidature in multifunctional, flexible electronic applications.

Declaration of Competing Interest

The authors declare that they have no known competing financial interests or personal relationships that could have appeared to influence the work reported in this paper.

Data Availability

Data will be made available on request.

Acknowledgment

SB acknowledges financial assistance from Department of Science and Technology (DST) funding DST/ NM/ NT/2020/322.

Appendix A. Supporting information

Supplementary data associated with this article can be found in the online version at doi:10.1016/j.snb.2023.133346.

References

[1] S. Veeralingam, S.S. Gunasekaran, S. Badhulika, Materials Chemistry Frontiers 6 (16) (2022) 2297–2308.
[2] D.K. Bharti, S. Veeralingam, S. Badhulika, Materials Horizons 9 (2) (2022) 663–674.
[3] S.-N. Chen, M.-Z. Huang, Z.-H. Lin, C.-P. Liu, Nano Energy 65 (2019), 104069.
[4] J.-S. Im, I.-K. Park, ACS Appl. Mater. Interfaces 10 (30) (2018) 25660–25665.
[5] M. Zhang, M. Zhao, M. Jian, C. Wang, A. Yu, Z. Yin, X. Liang, H. Wang, K. Xia, X. Liang, J. Zhai, Y. Zhang, Matter 1 (1) (2019) 168–179.
[6] W. Gong, C. Hou, J. Zhou, Y. Guo, W. Zhang, Y. Li, Q. Zhang, H, Nat. Commun. 10 (1) (2019) 868.
[7] J. Chen, Y. Huang, N. Zhang, H. Zou, R. Liu, C. Tao, X. Fan, Z.L. Wang, Nat. Energy 1 (10) (2016) 16138.
[8] L. Margulis, G. Salitra, R. Tenne, M. Talianker, Nature 365 (6442) (1993) 113–114.
[9] F.L. Deepak, R. Esparza, B. Borges, X. Lopez-Lozano, M. Jose-Yacaman, ACS Catal. 1 (5) (2011), 29.37-543.
[10] H. Li, Q. Zhang, C.C.R. Yap, B.K. Tay, T.H.T. Edwin, A. Olivier, D. Baillargeat, Adv. Funct. Mater. 22 (7) (2012) 1385–1390.
[11] J. Cao, D. Zhang, C. Gu, X. Zhang, M. Okhawilai, S. Wang, J. Han, J. Qin, Y. Huang, Nano Energy 89 (2021), 106322.
[12] Y.-E. Shin, J.-E. Lee, Y. Park, S.-H. Hwang, H.G. Chae, H. Ko, J. Mater. Chem. A 6 (45) (2018) 22879–22888.
[13] S. Veeralingam, S. Badhulika, ACS Applied Energy Materials 5 (10) (2022) 12884–12896.
[14] Z. Zhao, C. Yan, Z. Liu, X. Fu, L.-M. Peng, Y. Hu, Z. Zheng, Adv. Mater. 28 (46) (2016) 10267–10274.
[15] X. Bao, A.K. Abdala, E.N, Sensors 21 (1) (2021) 78.
[16] Q. Yue, Z. Shao, S. Chang, J. Li, Nanoscale Res. Lett. 8 (1) (2013) 1–7.
[17] B. Cho, M.G. Hahm, M. Choi, J. Yoon, A.R. Kim, Y.J. Lee, S.G. Park, J.D. Kwon, C. S. Kim, M. Song, Y. Jeong, Sci. Rep. 5 (1) (2015) 1–6.
[18] R. Kumar, W. Zheng, X. Liu, J. Zhang, M. Kumar, Adv. Mater. Technol. 5 (5) (2020), 1901062.
[19] T. Pham, G. Li, E. Bekyarova, M.E. Itkis, A. Mulchandani, ACS Nano 13 (3) (2019) 3196–3205.
[20] P. Sahatiya, S. Badhulika, J. Mater. Chem. C 5 (44) (2017) 11436–11447.
[21] Y. Kim, S.K. Kang, N.C. Oh, H.D. Lee, S.M. Lee, J. Park, H. Kim, ACS Appl. Mater. Interfaces 11 (42) (2019) 38902–38909.
[22] Y. Seekaew, W. Pon-On, C. Wongchoosuk, ACS Omega 4 (16) (2019) 16916–16924.
[23] J. van den Broek, D. Bischof, N. Derron, S. Abegg, P.A. Gerber, A.T. Güntner, S. E. Pratsinis, Anal. Chem. 93 (2) (2020) 1170–1178.
[24] B. Li, X. Zou, H. Wang, Y. Lu, C. Shen, Y. Chu, Anal. Biochem. 581 (2019), 113344.
[25] Y. Che, D.E. Gross, H. Huang, D. Yang, X. Yang, E. Discekici, Z. Xue, H. Zhao, J. S. Moore, L. Zang, J. Am. Chem. Soc. 134 (10) (2012) 4978–4982.
[26] D.J. Late, T. Doneux, M. Bougouma, Appl. Phys. Lett. 105 (23) (2014), 233103.
[27] J. Park, J. Mun, J.S. Shin, S.W. Kang, R. Soc. Open Sci. 5 (12) (2018), 181462.
[28] H. Yan, P. Song, S. Zhang, J. Zhang, Z. Yang, Q. Wang, Ceram. Int. 42 (7) (2016) 9327–9331.
[29] S. Sharma, A. Kumar, N. Singh, D. Kaur, Sens. Actuators B: Chem. 275 (2018) 499–507.

Sushmitha Veeralingam obtained her M.Tech (Nanoelectronics) from SASTRA University, Tanjore, India in 2017 and currently pursuing her Ph.D. from the Dept. of Electrical Engineering at IIT, Hyderabad. Her primary research interest includes Flexible electronics, 2D Nanomaterials, Device fabrication, point of care diagnostic systems and self-powering of flexible electronic devices using Nanogenerators.

Sushmee Badhulika obtained her B.Tech (Electrical Engineering) from National Institute of Technology, Rourkela, India in 2007 and her M.S and Ph.D from the Department of Electrical Engineering, University of California, Riverside, USA in 2009 and 2011 respectively. She is currently a Professor in the Dept. of Electrical Engineering at IIT, Hyderabad. Her primary research interests include Flexible electronics, Nanomaterials, devices and circuits with focus on developing chemical and electronic sensors for bio/chemical sensing and electronic applications.